Chemical Science

EDGE ARTICLE

Check for updates

An anti-thermal-quenching organic–inorganic hybrid manganese-based single-crystal scintillator for high-temperature X-ray imaging†

Jing-Hua Chen, Jian-Bin Luo, Zi-Lin He, Qing-Peng Peng, Jun-Hua Wei,* Zhi-Zhong Zhang, Xiu-Xian Guo and Dai-Bin Kuang [ID] *

High-temperature X-ray detection holds promising potential in practical applications in the development of industry. Organic–inorganic manganese-based halide (OIMH) scintillators have undergone a research upsurge due to their high X-ray attenuation ability, low preparation cost, outstanding photoluminescence performance, and flexible structures. However, the thermal quenching effects of OIMH materials limit their applications at high temperatures. Herein, we report two zero-dimensional OIMH scintillators, (4-NH$_3$TBP)MnBr$_4$ (4-NH$_3$TBP = 4-aminobutyl triphenylphosphonium) and (4-DMATBP)MnBr$_4$ (4-DMATBP = (4-(dimethylamino)butyl)triphenylphosphonium) single crystals, which were developed through rational molecular design. Their abnormal temperature-dependent luminescence behaviors under ultraviolet lamp excitation and X-ray irradiation are observed. Notably, the (4-DMATBP)MnBr$_4$ single crystal exhibits an anti-thermal-quenching effect under ultraviolet light and X-ray irradiation, which can be attributed to the participation of intrinsic crystal defects, rigid crystal structure and longer Mn–Mn distance. Density functional theory calculations further demonstrate that Br vacancies are responsible for the formation of the trap state. The (4-DMATBP)MnBr$_4$ scintillator exhibits an impressive light yield of 46 722 photon per MeV at 130 °C, indicating its feasibility for application in high-temperature X-ray detection. The transparent single crystal possesses a robust resolution of 42 lp mm^{-1} in X-ray imaging and shows high imaging quality at high temperatures.

Introduction

High-temperature scintillators have been widely used in petroleum exploration, space nuclear exploration, and reactors.[1–3] As the core of detectors, scintillators with high light output, excellent thermal stability, and resistance to pressure are required.[4–7] Traditional high-temperature scintillators (NaI:Tl$^+$, CsI:Tl$^+$, and LaBr$_3$:Ce^{3+}) and the commercially available scintillators (YAG:Ce^{3+}, SrSi$_2$O$_2$N$_2$:Eu^{2+}, and LuAG:Ce^{3+}) with low thermal quenching (TQ) show negligible emission loss, and have been applied to petroleum exploration.[3,8–10] However, the poor scintillation performance under extreme temperatures and high-cost synthesis processes of the above scintillators limit their applications.[11] Therefore, materials with excellent scintillation performance at high temperatures that can be prepared through facile low-temperature synthesis routes are needed.

Key Laboratory of Bioinorganic and Synthetic Chemistry of Ministry of Education, Lehn Institute of Functional Materials, GBRCE for Functional Molecular Engineering, School of Chemistry, IGCME, Sun Yat-Sen University, Guangzhou 510275, China. E-mail: weijh39@mail.sysu.edu.cn; kuangdb@mail.sysu.edu.cn

Organic–inorganic manganese halides (OIMHs) have attracted extensive research interest due to their low toxicity, flexible structures, and high emission quantum efficiency, and thus show great application prospects in light-emitting diodes (LEDs), X-ray scintillation, and anti-counterfeiting technologies.[12–15] OIMHs always possess a low-dimensional structure with highly localized excitons, which promotes radiative recombination and accounts for their high photoluminescence quantum yield (PLQY).[16] However, most OIMHs suffer from serious PL quenching as the temperature increases (>100 °C) due to the electron–photon-coupling-induced non-radiative relaxation,[17] hampering their application in high-temperature scintillation imaging. Anti-thermal quenching (ATQ) materials with minimal emission loss at elevated temperatures could meet the demands for commercial applications. Many research works towards obtaining ATQ OIMH materials have been carried out.[18] Notably, defect engineering and structural modulation are the most common strategies to realize ATQ properties.[19–22] Defect engineering can provide extra states that can serve as a carrier storage bank and release carriers to the emissive centers at higher temperatures. Moreover, structure modulation can affect the structural rigidity and symmetric sites through chemical substitution, further regulating the emission behaviors.[18]

Yang's group synthesized a $(TTPhP)_2MnCl_4$ ($TTPhP^+$ = tetraphenylphosphonium cation) material with an ATQ effect through organic cation engineering; the material shows a low thermal quenching effect up to 200 °C under ultraviolet (UV) light (the maximum intensity is about 1.2 times higher than the initial intensity) and a weak TQ property under X-ray irradiation.[23] Very recently, Xu and coauthors successfully prepared a 1D $Cs_5Cu_3Cl_6I_2$ scintillator by adjusting the ratio of Cl^- and I^-; the scintillator exhibits slight emission loss when being heated to 160 °C.[24] However, the low optical transmittance and severe light scattering of the above scintillator screens deteriorate their X-ray imaging performance. The X-ray imaging resolution of the $(TTPhP)_2MnCl_4$ and $Cs_5Cu_3Cl_6I_2$ scintillator screens can only reach 4 lp mm^{-1} at 200 °C and nearly 18 lp mm^{-1} at 150 °C, respectively.[23,24] The unsatisfactory X-ray imaging resolution can be ascribed to the TQ properties of the above materials during the heating process under X-ray irradiation. In terms of high-resolution X-ray imaging, single-crystal perovskite scintillators have been praised for their high transparency, strong X-ray attenuation capability, suppressed light scattering, excellent X-ray energy response, and low detection limit.[12,25–27] Therefore, an optically transparent single crystal scintillator with weak TQ would be attractive for high-temperature X-ray detection and imaging.

Recent advances in OIMHs have focused on tailoring triphenylphosphine derivatives through strategic functionalization with alkyl chains, rigid phenyl groups, and alkoxy groups to enhance their luminescence properties.[28–31] Notably, the introduction of amine functionalities to these systems remains underexplored despite their potential to modulate electronic structures through protonation effects. To address this gap, we designed a novel series of butyltriphenylphosphonium salts incorporating amine cations at the alkyl chain termini. Interestingly, different from the reported monoprotonated structures, the as-synthesized organic salts are diprotonated. This unique protonation state induces enhanced thermal stability, as evidenced by their glass transition temperatures (T_g) exceeding those of reported OIMHs crystals,[14,30,32] which is conducive to subsequent scintillation application of the OIMH glass.

In this work, we successfully synthesized two OIMH single crystal scintillators through introducing two methyl ($-CH_3$) groups at the end of the alkyl chain of the organic cation, which adjusted the rigidity and anion–cation interactions. The (4-NH_3TBP)MnBr$_4$ single crystal (4-NH_3TBP = 4-aminobutyl triphenylphosphonium) has a weak TQ effect, while the (4-DMATBP)MnBr$_4$ single crystal (4-DMATBP = (4-(dimethylamino)butyl) triphenylphosphonium) possesses ATQ properties. Both crystals exhibit green emission under UV light and X-ray radiation, as well as high thermal stability. Notably, the (4-DMATBP)MnBr$_4$ single crystal exhibits an ATQ effect and attains enhancement within the temperature range of 30–200 °C; the maximum intensity is 3.85 times higher than the initial intensity under UV excitation. Moreover, the light yield of the (4-DMATBP)MnBr$_4$ single crystal reaches 46 722 photon per MeV at 130 °C due to its ATQ properties under X-ray irradiation, which is 3.19 times higher than that at 30 °C. Such a significant

radioluminescence (RL) improvement with increasing temperature under X-ray excitation has rarely been reported. The ATQ effect can be mainly attributed to its rigid crystal structure, longer Mn–Mn distance, and the participation of trap states, according to the single-crystal X-ray diffraction (SCXRD), electron paramagnetic resonance (EPR), thermoluminescence (TL), and density functional theory (DFT) results. Additionally, the transparent (4-DMATBP)MnBr$_4$ single crystal shows a high spatial resolution of up to 42 lp mm^{-1} for X-ray imaging at room temperature and exhibits high-quality imaging at high temperatures.

Results and discussion

Synthesis and characterization of OIMH single crystals

The organic phosphonium salts were synthesized via a facile reflux reaction procedure (ESI Scheme 1, please see the ESI for experimental details†). White crystalline products with blue emission were obtained through recrystallization (Fig. S1a, b, S2a and b†). Attenuated total reflection Fourier-transform infrared (ATR-FTIR) and NMR measurements verified that the target products had been successfully synthesized (Fig. S1c, d, S2c and d†). The difference between 4-NH$_3$TBPBr and 4-DMATBPBr lies in the methyl functional groups attached to the terminal N atom. As shown in Fig. S3a and b,† single-crystal X-ray diffraction measurement (SCXRD) revealed that the 4-NH$_3$-TBPBr crystal adopts a triclinic crystal structure, while 4-DMATBPBr crystallizes in a monoclinic space group (Table S1†). The powder X-ray diffraction (PXRD) patterns of the ground powders are consistent with the simulated results based on the SCXRD data (Fig. S3c†), indicating the successful preparation of the functional phosphonium salts in high purity. The thermal properties of 4-NH$_3$TBPBr and 4-DMATBPBr were evaluated through thermogravimetric analysis (TGA) and differential scanning calorimetry (DSC). As shown in Fig. S4 and Table S2,† the melting temperature (T_m) and decomposition temperature (T_d) of 4-DMATBPBr were higher than those of 4-NH$_3$TBPBr, indicating that the introduction of the –CH$_3$ groups improved the thermal stability.

Mn-based metal halide crystals of (4-NH$_3$TBP)MnBr$_4$ and (4-DMATBP)MnBr$_4$ were grown through the solvent evaporation method (please see the Synthesis section in the ESI†). Intriguingly, the (4-DMATBP)MnBr$_4$ crystals tended to grow as laminar single crystals with a maximum size of 5 mm × 7 mm × 0.5 mm via slow solvent evaporation in a CH$_3$OH and HBr solution (ESI Scheme 2†). The crystal structures of (4-NH$_3$TBP)MnBr$_4$ and (4-DMATBP)MnBr$_4$ were determined via SCXRD measurements, and the detailed crystallographic data are available in Tables S1 and S3.† The (4-NH$_3$TBP)MnBr$_4$ crystal adopts the triclinic $P\bar{1}$ space group, whereas (4-DMATBP)MnBr$_4$ crystallizes in the monoclinic space group $P2_1/n$. The crystallographic asymmetric units of (4-NH$_3$TBP)MnBr$_4$ and (4-DMATBP)MnBr$_4$ are shown in Fig. S5,† in which one Mn atom is coordinated by four Br atoms to form a $[MnBr_4]^{2-}$ tetrahedral cluster. The $[MnBr_4]^{2-}$ tetrahedral clusters are separated by the organic cations, giving rise to zero-dimensional structures for both (4-NH$_3$TBP)MnBr$_4$ and (4-DMATBP)MnBr$_4$ (Fig. 1a and b).
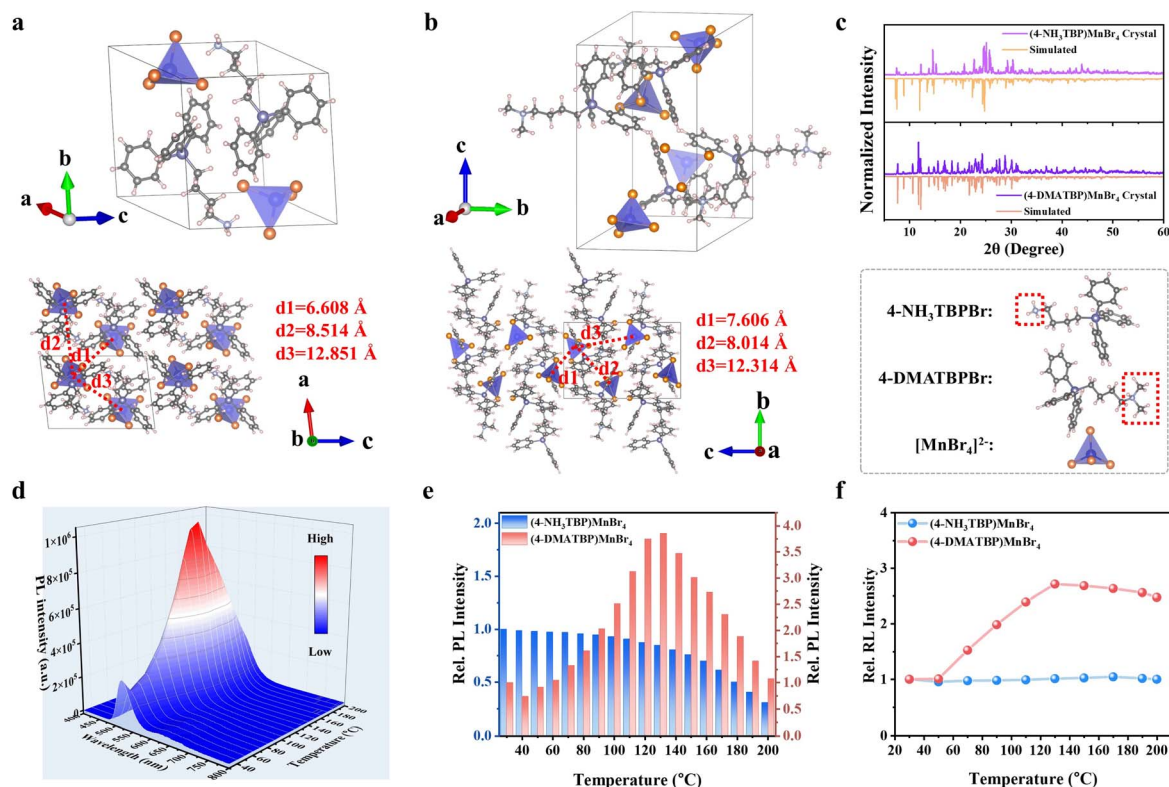
Fig. 1 Single-crystal structures and temperature-dependent luminescence properties. Crystal structures of (a) the (4-NH_3TBP)$MnBr_4$ and (b) (4-DMATBP)$MnBr_4$ crystals (pink: H, grey: C, light purple: N, orange: Br, purple: P, blue: Mn). (c) Comparison of the simulated and experimental XRD patterns of the (4-NH_3TBP)$MnBr_4$ and (4-DMATBP)$MnBr_4$ crystals. (d) Temperature-dependent PL spectra of the (4-DMATBP)$MnBr_4$ crystal. (e) Temperature-dependent normalized integrated PL intensity of (4-NH_3TBP)$MnBr_4$ and (4-DMATBP)$MnBr_4$ crystals under 360 nm light excitation upon being heated to 200 °C. (f) Temperature-dependent normalized integrated RL intensity of (4-NH_3TBP)$MnBr_4$ and (4-DMATBP)$MnBr_4$ crystals upon being heated to 200 °C.

Notably, the shortest Mn–Mn distances in the (4-NH_3TBP)$MnBr_4$ and (4-DMATBP)$MnBr_4$ crystals are 6.608 Å and 7.606 Å, respectively. PXRD measurement proved the high phase purity of the as-synthesized single crystals *via* comparison to the simulated results (Fig. 1c). Thermogravimetric analysis (TGA) and differential scanning calorimetry (DSC) measurements were performed to investigate the thermal properties of the crystals. As shown in Fig. S6 and Table S4,† the T_d values of the (4-NH_3TBP)$MnBr_4$ and (4-DMATBP)$MnBr_4$ crystals are 288 and 314 °C, while their T_m values are 244 and 262 °C, respectively. The thermal analysis illustrates that the crystals remain in the solid state below 200 °C.

Optical properties of the OIMH single crystals

The ultraviolet-visible spectra of the OIMH crystals in Fig. S7† show several groups of peaks in the range of 250–500 nm, which originate from the d–d transitions of Mn^{2+}. The bands at 294, 365, 377, 438, 450, and 460 nm correspond to the electronic transitions of Mn^{2+} from the ground state $^6A_1$ to the excited states $^4T_1(F)$, $^4E(D)$, $^4T_2(D)$, $^4A_1/^4E(G)$, $^4T_2$ (G), and $^4T_1$ (G), respectively.[33] The photoluminescence excitation (PLE) and PL spectra of the Mn-based crystals were obtained and shown in Fig. S8a and b.† The (4-NH_3TBP)$MnBr_4$ and (4-DMATBP)$MnBr_4$ crystals both exhibit green emission from the $^4T_1 \rightarrow {}^6A_1$

transition of Mn^{2+} in a typical tetrahedral coordination geometry (Fig. S8c and d†). Furthermore, the (4-NH_3TBP)$MnBr_4$ crystal shows a brighter greenish emission peak at 519 nm with a PLQY of 63.5% and a full width at half maximum (FWHM) of 50 nm. In contrast, the (4-DMATBP)$MnBr_4$ crystal shows an emission peak at 520 nm with a FWHM of 45 nm and a lower PLQY of 26.9% at room temperature (Fig. S8e†). The time-resolved PL (TRPL) spectra of (4-NH_3TBP)$MnBr_4$ and (4-DMATBP)$MnBr_4$ crystals indicate average lifetimes of 276 and 125 μs, respectively (Fig. S9†).

The temperature-dependent luminescence spectra of (4-NH_3TBP)$MnBr_4$ and (4-DMATBP)$MnBr_4$ crystals under 360 nm ultraviolet light and X-ray excitation were collected to investigate the emissive mechanism. As shown in Fig. 1d and S10a,† the PL intensity of the (4-DMATBP)$MnBr_4$ crystal increases with temperature, while (4-NH_3TBP)$MnBr_4$ exhibits a decreasing trend as the temperature rises. As displayed in Fig. 1e, the temperature-dependent integrated PL intensity of the (4-DMATBP)$MnBr_4$ crystal reaches a maximum at 130 °C, which is 3.85 times higher than the initial intensity at 30 °C. The temperature-dependent PLQY measurement shown in Fig. S10b† reveals a trend consistent with the temperature-dependent PL intensity, achieving a maximum PLQY value of 98.60% at 130 °C. However, the PLQY of (4-NH_3TBP)$MnBr_4$

exhibits a decreasing trend consistent with the weak TQ effect under ultraviolet light excitation. Notably, the temperature-dependent integrated RL intensity under X-ray irradiation suggests that $(4\text{-}NH_3TBP)MnBr_4$ exhibits a nearly zero-TQ effect up to 200 °C, whereas the $(4\text{-}DMATBP)MnBr_4$ crystal shows an ATQ effect (Fig. 1f and S11†). Additionally, the RL intensity of $(4\text{-}DMATBP)MnBr_4$ reaches a maximum at 130 °C, which is 1.71 times greater than that at room temperature. Therefore, the prepared Mn-based halide crystals exhibit great potential for application at high temperatures.

Radioluminescence properties of scintillators

To investigate the radioluminescence properties, we further evaluated the performance of the two single-crystal scintillators, including their light yield (LY) and limit of detection (LOD). As displayed in Fig. 2a, the two OIMHs exhibit analogous X-ray absorption coefficients (α) slightly lower than those of the all-inorganic scintillators. The X-ray source used for the test exhibits a characteristic peak and photon energy of 22 keV (Fig. S12†). The attenuation efficiency of $(4\text{-}NH_3TBP)MnBr_4$ and $(4\text{-}DMATBP)MnBr_4$ at an X-ray energy of 22 keV (Fig. 2b) shows that they can absorb nearly 100% of the X-rays at a thickness of 1 mm. To derive the light yield (LY) values of $(4\text{-}NH_3TBP)MnBr_4$ and $(4\text{-}DMATBP)MnBr_4$, the commercially available LuAG:Ce crystal was selected as a reference scintillator (LY = 25 000 photon per MeV). To minimize morphology-dependent differences in the RL measurement, the samples were pressed into wafers of the same size as the standard scintillator. The light yields of $(4\text{-}NH_3TBP)MnBr_4$ and $(4\text{-}DMATBP)MnBr_4$ were calculated to be 36 572 photon per MeV and 14 663 photon per MeV, respectively (Fig. 2c).

Notably, the light yield of $(4\text{-}DMATBP)MnBr_4$ crystal reaches a maximum of 46 722 photon per MeV at 130 °C, which is 3.19 times higher than that at room temperature (Fig. 2d). $(4\text{-}NH_3TBP)MnBr_4$ also demonstrates excellent performance with a high LY value of about 40 000 photon per MeV within the temperature range of 30 °C to 200 °C (Fig. 2e). The higher light yields at high temperatures support their application in high-temperature detection scenarios.

The limit of detection (LOD) is a crucial parameter for scintillators. A photomultiplier tube (PMT) was employed to record the light output under low-dose-rate X-ray irradiation. As shown in Fig. 2f and S13,† the LuAG:Ce standard scintillator and the two OIMH single crystals exhibit a linear dependence between the RL intensity and the X-ray dose rates. The LOD of LuAG:Ce was derived to be 39.01 nGy s^{-1}, while those of the $(4\text{-}NH_3TBP)MnBr_4$ and $(4\text{-}DMATBP)MnBr_4$ crystals are 12.66 nGy s^{-1} and 46.15 nGy s^{-1}. All the measured LODs are below the standard for medical imaging (5.5 μGy s^{-1}); such low LOD values are advantageous for obtaining high-quality X-ray images.[34]

Luminescence properties and crystal structure

In order to clarify the differences in the luminescence properties of the single crystals, we measured the Mn–Mn distance in the OIMHs, since a longer Mn–Mn distance would afford
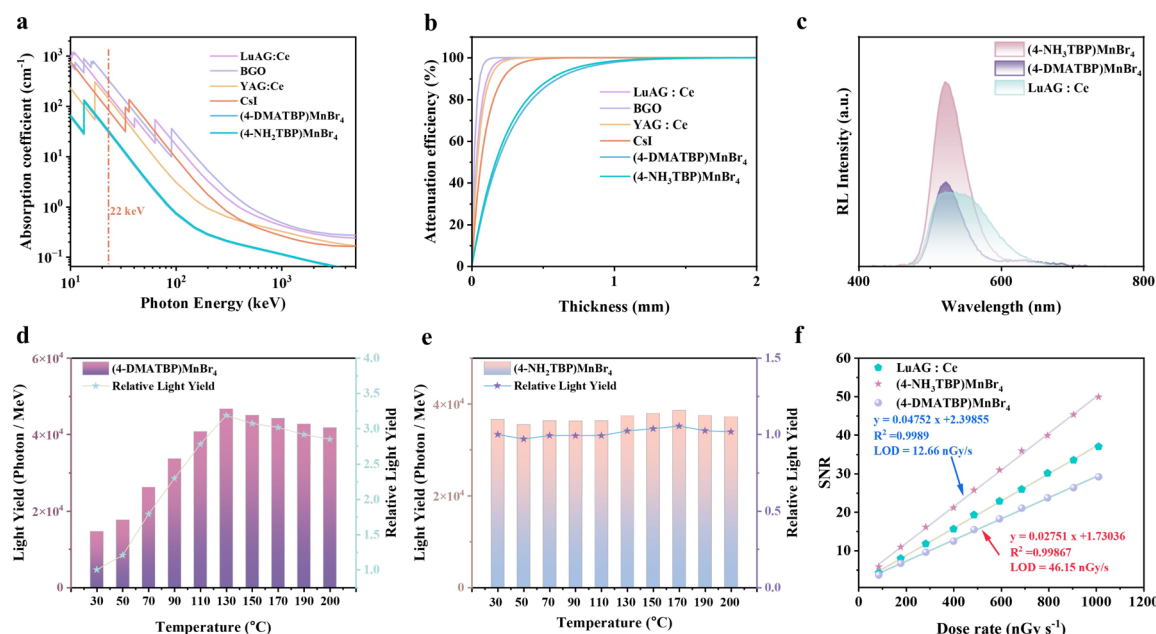

Fig. 2 X-ray scintillation performance characterization of $(4\text{-}NH_3TBP)MnBr_4$ and $(4\text{-}DMATBP)MnBr_4$ crystals. (a) Absorption coefficients of $(4\text{-}NH_3TBP)MnBr_4$ and $(4\text{-}DMATBP)MnBr_4$ crystals, as well as those of LuAG:Ce, BGO, YAG:Ce, CsI, as a function of photon energy. (b) Thickness-dependent attenuation efficiency of the above crystals under 22 keV X-ray irradiation. (c) RL spectra of $(4\text{-}NH_3TBP)MnBr_4$ and $(4\text{-}DMATBP)MnBr_4$ crystals and a commercial LuAG:Ce scintillator under X-ray excitation (40 kV, 100 μA). Temperature-dependent light yields of (d) $(4\text{-}DMATBP)MnBr_4$ and (e) $(4\text{-}NH_3TBP)MnBr_4$ crystals within the temperature range of 30 to 200 °C. (f) Linear relationship between RL intensity and X-ray irradiation dose rates of $(4\text{-}NH_3TBP)MnBr_4$ and $(4\text{-}DMATBP)MnBr_4$ crystals, as well as that of the standard scintillator LuAG:Ce; the corresponding LOD was determined as the dose rate at which the SNR is equal to 3.
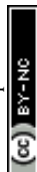
a higher PLQY due to the concentration quenching effect.[23,35,36] However, the shortest Mn–Mn distances of the $(4\text{-NH}_3\text{TBP})\text{MnBr}_4$ and $(4\text{-DMATBP})\text{MnBr}_4$ crystals are 6.608 Å and 7.606 Å, while their PLQY values are 63.5% and 26.9%, respectively, indicating that the Mn–Mn distance is not the major factor affecting the PLQY of the two OIMH single crystals.

It has been reported that the emission efficiency can be regulated by tuning weak interactions to suppress non-radiative transitions. Therefore, inhibiting the motion of the $[\text{MnBr}_4]^{2-}$ anions could result in a higher PLQY by decreasing the non-radiative transitions.[37,38] As shown in Fig. S14,† SCXRD measurement demonstrated that the $[\text{MnBr}_4]^{2-}$ anions in the $(4\text{-NH}_3\text{TBP})\text{MnBr}_4$ crystal are fully ordered while those in the $(4\text{-DMATBP})\text{MnBr}_4$ crystal are relatively disordered over four positions. Hirshfeld surface calculations were performed using the CrystalExplorer package to shed more light on the weak interactions between $[\text{MnBr}_4]^{2-}$ and the surrounding cations.[39] The 2D fingerprint plots in Fig. S15a and b† show the substantial differences between the Br–H interactions in these two OIMH compounds. The cyan-blue area in the red box clearly indicates the stronger Br···H–C(N) interactions between $[\text{MnBr}_4]^{2-}$ and the organic cations in $(4\text{-NH}_3\text{TBP})\text{MnBr}_4$ compared with those in the $(4\text{-DMATBP})\text{MnBr}_4$ crystal, possibly originating from the three hydrogen atoms of the $-\text{NH}_3$ group at the end of the cation. Additionally, we measured the Mn···H–C (N) bond length between $[\text{MnBr}_4]^{2-}$ and the organic cations to evaluate the interaction distance between the anions and cations (Tables S5 and 6†). The calculated average Mn···H distances for the $(4\text{-NH}_3\text{TBP})\text{MnBr}_4$ and $(4\text{-DMATBP})\text{MnBr}_4$ crystals are 8.19 and 8.64 Å, suggesting a shorter interaction distance and stronger interaction between anions and cations

in the $(4\text{-NH}_3\text{TBP})\text{MnBr}_4$ crystal. Overall, the motion of $[\text{MnBr}_4]^{2-}$ in $(4\text{-NH}_3\text{TBP})\text{MnBr}_4$ is restricted due to the pronounced anion–cation interactions. The more rigid structure of $(4\text{-NH}_3\text{TBP})\text{MnBr}_4$ reduces the thermal vibration of $[\text{MnBr}_4]^{2-}$ and suppresses the non-radiative transition, affording an improved PLQY.

As $(\text{TPPen})_2\text{MnBr}_4$ (TPPen = pentyltriphenylphosphonium)[40] has a similar structure to $(4\text{-NH}_3\text{TBP})\text{MnBr}_4$ and $(4\text{-DMATBP})\text{MnBr}_4$, we compared their Br–H interactions. The interaction distance between anions and cations in the $(\text{TPPen})_2\text{MnBr}_4$ crystal is longer than those of the present two compounds, indicating that the introduction of the N atom and methyl groups shortens the interaction distance and leads to stronger interactions (Fig. S15c†). Moreover, the N atom provides a cationic center, resulting in the longer shortest Mn–Mn distance.[35] Thus, the $(4\text{-NH}_3\text{TBP})\text{MnBr}_4$ and $(4\text{-DMATBP})\text{MnBr}_4$ crystals have more rigid structures. As reported, rigid crystal structures can reduce emission loss during the heating process, leading to weak TQ behavior.[41]

Exploration of the anti-thermal-quenching mechanism of the luminescence of the $(4\text{-DMATBP})\text{MnBr}_4$ crystal

To clarify the mechanism of the anti-thermal quenching behavior in the $(4\text{-DMATBP})\text{MnBr}_4$ crystal, we performed temperature-dependent XRD, high-temperature SCXRD, TL, EPR, and temperature-dependent TRPL. The temperature-dependent XRD (Fig. 3a) results illustrate that no phase transition is observed when the $(4\text{-DMATBP})\text{MnBr}_4$ crystal is heated to 200 °C, in good agreement with the DSC results. Furthermore, single-crystal structures were collected at several
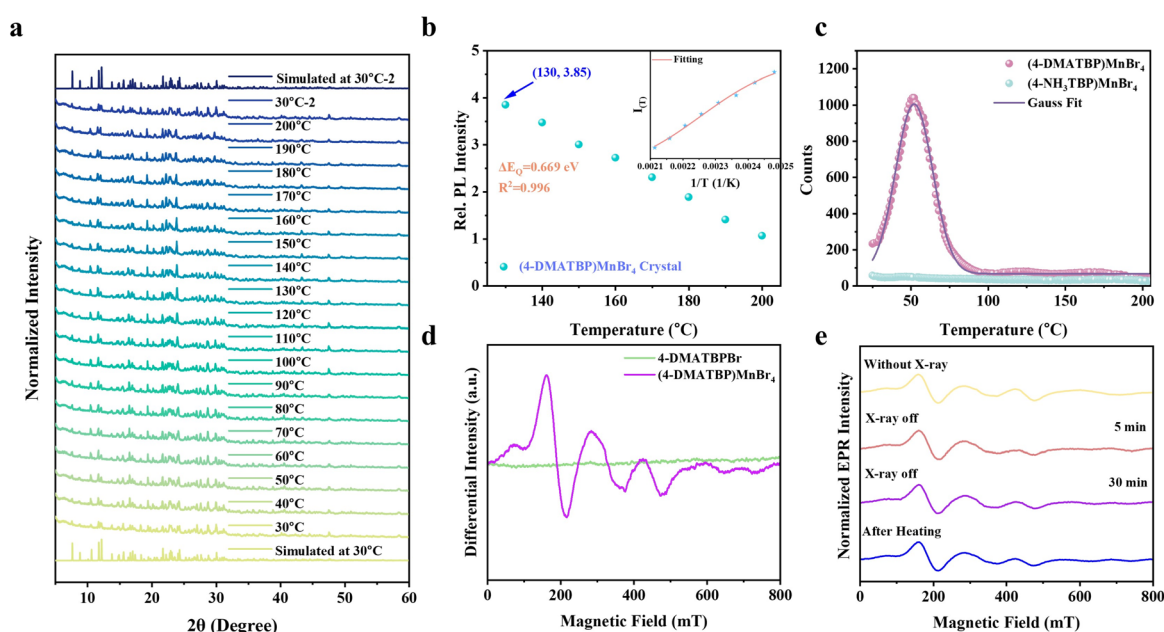

Fig. 3 Correlation mechanistic investigation of fluorescence properties. (a) Temperature-dependent XRD patterns of the $(4\text{-DMATBP})\text{MnBr}_4$ crystal in the range of 30 to 200 °C and returning to 30 °C after being heated to 200 °C. (b) Nonlinear fitting of the normalized integrated PL intensity of the $(4\text{-DMATBP})\text{MnBr}_4$ crystal. (c) TL curves of $(4\text{-NH}_3\text{TBP})\text{MnBr}_4$ and $(4\text{-DMATBP})\text{MnBr}_4$ crystals pre-irradiated under X-ray irradiation. (d) EPR spectra of 4-DMATBPBr and $(4\text{-DMATBP})\text{MnBr}_4$ crystals. (e) EPR spectra of $(4\text{-DMATBP})\text{MnBr}_4$ crystals after different treatments.

temperatures and refined (Table S7†). The crystal structure remained unchanged, suggesting that the ATQ trend in the luminescence intensity is independent of phase transition. Additionally, the shortest Mn–Mn distances and average Mn–Br bond lengths at the corresponding temperatures are listed in Table S8.† It is evident that both the volume and the shortest Mn–Mn distance increase as temperature rises due to lattice expansion. The increasing Mn–Mn distance could suppress the energy transfer process between Mn atoms, thus inhibiting concentration quenching at high temperatures.[23] This could be further supported by the fact that the longer shortest Mn–Mn distance in the (4-DMATBP)MnBr$_4$ crystal compared with that in (4-NH$_3$TBP)MnBr$_4$ leads to a weaker TQ effect. Thus, the ATQ property of the (4-DMATBP)MnBr$_4$ crystal could be attributed to the longer Mn–Mn distance.

The observed PL intensity of (4-DMATBP)MnBr$_4$ first increases (303–403 K) and then decreases (>403 K) with increasing temperature. To obtain the charge carrier dynamics and the activation energy of thermal quenching, the following equation was applied for fitting:[23,42,43]

$$I_{(T)} = \frac{I_0}{1 + A \exp\left(-\dfrac{\Delta E_{\mathrm{Q}}}{\kappa T}\right)}$$

where I_0 corresponds to the intensity of photoluminescence at $T = 0$ K, $I(T)$ represents the emission intensity at an increasing temperature T, A is a coefficient, ΔE_{Q} refers to the thermal activation energy, and κ is the Boltzmann constant. The temperature-dependent PL of (4-DMATBP)MnBr$_4$ crystal can be fitted well by this model within the temperature range of 130–200 °C. As shown in Fig. 3b, ΔE_{Q} was calculated to be 0.669 eV; this high thermal activation energy accounts for the suppressed non-radiative recombination at higher temperature.

It has been reported that thermally-activated energy transfer from the trap state to the emissive state plays a vital role in abnormal thermally enhanced PL behavior.[3,21,42,44] Subsequently, we performed TL measurements to further investigate the trap state. As presented in Fig. 3c, no obvious peak appeared for (4-NH$_3$TBP)MnBr$_4$ while a peak at 52 °C was observed for the (4-DMATBP)MnBr$_4$ crystal. Through fitting the TL curve with a Gaussian function, the trap energy level was estimated to be 0.65 eV via the following equation:

$$E_{\mathrm{trap}} = T_{\max}/500$$

where $T_{\max}$ represents the temperature of the peak center.[42] Temperature-dependent TRPL measurements (Fig. S16 and Table S9†) further revealed that the average lifetimes of (4-DMATBP)MnBr$_4$ first increase with increasing temperature and then decrease gradually, which is consistent with the temperature-dependent PL spectra. In particular, the decay lifetime of (4-DMATBP)MnBr$_4$ reaches a maximum of 254 μs at 130 °C, which is nearly twice as long as the initial lifetime (125 μs). The results suggest that the process of carriers being trapped and detrapped from the trap level to the emissive state leads to a longer lifetime[11] and enhanced emission with increasing temperature.

EPR measurement can provide more information about the trap states in crystals; thus, we conducted EPR measurements of the as-synthesized compounds. As shown in Fig. 3d and S17,† the pure phosphonium salts exhibit no signal in their EPR spectra, while the as-prepared OIMH crystals present greatly different spectra. Notably, the spectrum of (4-NH$_3$TBP)MnBr$_4$ demonstrates only one resonance line, whereas the spectrum of (4-DMATBP)MnBr$_4$ is complicated and consists of numerous contributions. The EPR signals in the OIMHs originate from Mn^{2+}, as the pure phosphonium salts are EPR-silent. The EPR spectrum of (4-DMATBP)MnBr$_4$ was fitted using the spin Hamiltonian function (see the EPR measurements section in ESI† for details).[45] The fitting result is displayed in Fig. S18,† and matches well with the experimental data. The EPR results indicate that the local surroundings of the Mn^{2+} in (4-DMATBP)MnBr$_4$ are quite different from those in (4-NH$_3$TBP)MnBr$_4$. Considering the similar structure of these two crystals, this is possibly due to nearby defects. Additionally, we further performed EPR spectroscopy of the crystals after subjecting them to different treatments. As shown in Fig. 3e, the EPR spectra of the crystals after X-ray irradiation and heating exhibit the same profiles as the untreated ones do, confirming that the trap states originate from intrinsic defects in the (4-DMATBP)MnBr$_4$ crystal.

DFT calculations were performed to reveal the defect type, and several possible vacancy structures were proposed. As shown in Fig. S19,† the possible vacancy defect structures include four different Br vacancies, [MnBr$_4$]$^{2-}$ vacancy, and organic (C$_{24}$H$_{30}$NP$^+$) vacancy. The density of states (DOS) and projected DOS (PDOS) calculations were plotted to determine the major contributions to the conduction band minimum (CBM) and valence band maximum (VBM). As shown in Fig. 4a,
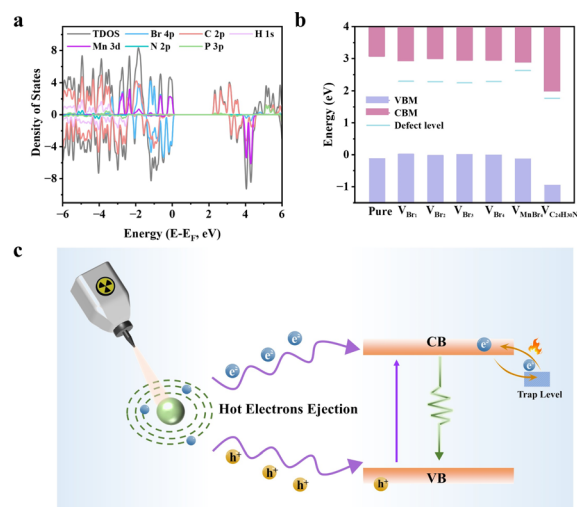

Fig. 4 Proposed mechanism of anti-thermal-quenching behavior of the luminescence under X-ray irradiation. (a) DOS and partial DOS plots for the (4-DMATBP)MnBr$_4$ crystal. (b) Energy diagram of the pure (4-DMATBP)MnBr$_4$ crystal and possible vacancy defects. The values of VBM, CBM, and defect levels are derived from the corresponding density of states. (c) Possible mechanism of anti-thermal-quenching property of the luminescence.

in the perfect (4-DMATBP)MnBr$_4$ crystal, the density states of the VBM are mainly contributed by Mn-d orbitals and C-p orbitals, while the C-p orbitals and P-p orbitals are dominant in the CBM for spin-up states. However, for the spin-down states, the Br-p orbitals and C-p orbitals primarily contribute to the VBM, which is quite different from the case for the spin-up states. The asymmetric DOS diagram indicates the ferromagnetic nature of the (4-DMATBP)MnBr$_4$ crystal.[46]

Fig. S20† shows the DOS and PDOS plots corresponding to the six possible vacancy defect structures in contrast to the perfect crystal structure. The defect levels corresponding to the different structure defects are shown in Fig. 4b and S21† for the spin-up and spin-down states. Notably, shallow and deep trap levels can be introduced in the different structure defects. For the spin-down states, the ΔE_{trap} (the energy gap between defect levels and CBM) values for V_{Br_1} to V_{Br_4} were distributed over a wide range of 0.64 to 0.72 eV, while for V_{MnBr_4} and $V_{C_{24}H_{30}NP}$, they were 0.24 and 0.28 eV, respectively. However, for the spin-up states, the ΔE_{trap} values for the different structure defects are in the range of 0.09 to 0.28 eV. Considering that halogen defects are widely present in metal halides,[21,42] the Br-vacancy structure was regarded as the most probable defect contributing to the trap level. Moreover, the calculated trap state level of V_{Br} is close to the TL result (0.65 eV), further suggesting the possibility of V_{Br} in the crystal structure.

Based on the above analysis, we proposed a possible mechanism for the luminescence under ultraviolet excitation and X-ray irradiation. In the (4-NH$_3$TBP)MnBr$_4$ crystal, the rigid crystal structure inhibits the non-radiative recombination process of the crystal at high temperatures, leading to negligible emission loss as the temperature increases. However, for the (4-DMATBP)MnBr$_4$ crystal, the trap level makes a significant contribution. The rigid crystal structure and the longer shortest Mn–Mn distance of the (4-DMATBP)MnBr$_4$ crystal inhibit concentration quenching at high temperatures, which is beneficial to the ATQ effect. Additionally, carriers will be trapped by the trap states, which can then serve as a carrier bank. As shown in Fig. 4c, the luminescence intensity is enhanced as the temperature increases due to the release of carriers from trap states to the emissive state of Mn^{2+}, resulting in the ATQ effect. Notably, under different excitation light sources, the anti-thermal quenching effect of the emission behavior is not all the same. Under X-ray irradiation, the atoms will be ionized through the photoelectric effect, and the electrons in the inner shell of the atoms will be excited and ejected out of the atoms, forming hot electrons and deep holes. Then, some amount of free excitons will be generated in the conduction and valence bands.[47] However, under ultraviolet (UV) light excitation, the valence electrons are excited to the excited state and return to the ground state to generate the green emission. The different relaxation and photophysical processes would result in the different temperature-dependent PL and RL intensities.

X-ray imaging of single-crystal scintillators

Due to their excellent scintillation performance and high optical transparency, the prepared OIMH single crystals can be employed as high-quality X-ray imaging materials. The crystals were also ground and pressed as polycrystalline wafers with a thickness similar to that of the single crystal. However, the preparation of a transparent (4-NH$_3$TBP)MnBr$_4$ single crystal with large size was difficult, and thus its X-ray imaging is not discussed. As shown in Fig. S22,† the polycrystalline wafers show low transmittance owing to the pronounced light scattering;[26,48] the transmittance of the (4-DMATBP)MnBr$_4$ wafer is approximately 50% in the range of 500–800 nm and that of the (4-NH$_3$TBP)MnBr$_4$ wafer reaches only 40%. The (4-DMATBP)MnBr$_4$ wafer with a spatial resolution of 8 line pair per millimeter (lp mm^{-1}) shows higher X-ray imaging quality than the (4-NH$_3$TBP)MnBr$_4$ wafer (Fig. S23†). The X-ray imaging resolution of the (4-DMATBP)MnBr$_4$ single crystal (∼0.5 mm thick) was measured to be 30 lp mm^{-1}, which is much higher than that of the wafer (Fig. 5a). Furthermore, the copper mesh with a rib pitch of 12 μm (namely, 42 lp mm^{-1}) can be clearly distinguished, highlighting its application potential in high-quality X-ray imaging (Fig. 5b). Moreover, as shown in Fig. 5c, the obvious gray value change proves the high imaging quality, indicating that the X-ray imaging resolution can reach up to 42 lp mm^{-1}.

Based on its ATQ behavior under X-ray irradiation, the as-synthesized (4-DMATBP)MnBr$_4$ single crystal was applied for high-temperature X-ray imaging. As demonstrated in Fig. 5d, the greenish emission intensity under 365 nm ultraviolet excitation first gradually becomes stronger and then decreases slightly with increasing temperature. Moreover, the single crystal maintains its high transmittance, as evidenced by the sharp visibility of the letter "K". Subsequently, the focused images of a copper mesh at different temperatures under X-ray irradiation are shown in Fig. 5e. The self-built X-ray imaging system is demonstrated in Fig. 5f. Benefitting from the high optical transparency of up to 95% (Fig. 5g), the X-ray images exhibit high contrast during the heating process (Fig. 5h). Notably, the single-crystal scintillator could give clear resolution, and there is no obvious reduction in the contrast of images in the range of 30–200 °C (Fig. S24†). To further investigate the X-ray imaging quality at high temperature, we selected two miniature electronic components as the imaging objects and performed X-ray imaging experiments (Fig. S25†). The structures of electronic components at variable temperatures can be recognized, demonstrating the (4-DMATBP)MnBr$_4$ single crystal to be an ideal candidate for high-temperature X-ray imaging with high quality. Notably, the wires connecting the pins, indicated by the white arrows, are clearly distinguishable during the heating process. For comparison, we systematically evaluated the commercial LuAG:Ce scintillator under the same temperatures. LuAG:Ce exhibits a spatial resolution approaching nearly 25 lp mm^{-1} at room temperature (Fig. S26a†). Moreover, similar to the (4-DMATBP)MnBr$_4$ single crystal, the LuAG:Ce scintillator demonstrates excellent X-ray imaging performance at elevated temperatures (Fig. S26b–e†). When observing the images of the copper mesh at various temperatures under X-ray irradiation using LuAG:Ce, there are no significant alterations, and the decrease in image contrast is hardly noticeable (Fig. S26b–d†). Likewise, Fig. S26e† presents
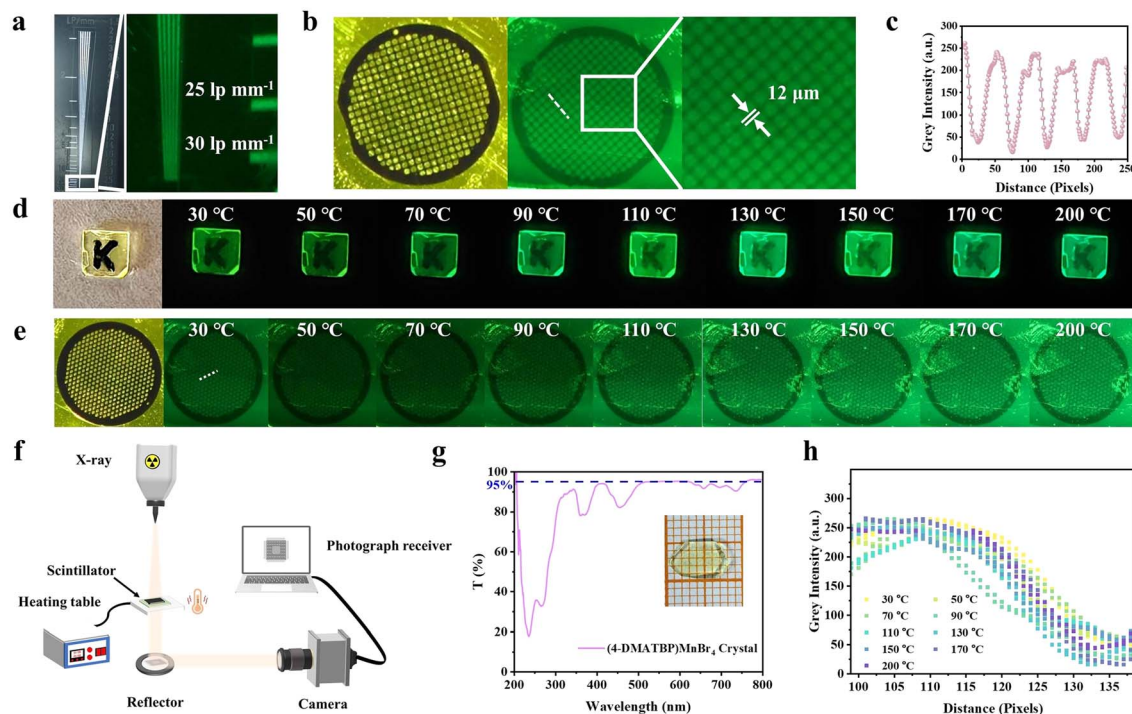
Fig. 5 X-ray imaging of the (4-DMATBP)MnBr$_4$ single crystal. (a) X-ray imaging of a lead-made line pair card at room temperature. (b) X-ray images of the copper mesh with a rib pitch of 12 μm (X-ray dose rate: 4.98 mGy s^{-1}). (c) Change in the gray values along the dashed line. (d) Optical images of the (4-DMATBP)MnBr$_4$ crystal under an ultraviolet lamp (365 nm) at different temperatures. (e) Temperature-dependent X-ray images of a copper mesh (rib pitch: 20 μm). (f) Schematic diagram of the high-temperature X-ray imaging device. (g) Transmittance plot of the (4-DMATBP)MnBr$_4$ crystal. (h) Gray value changes of the (4-DMATBP)MnBr$_4$ crystal along the dotted line in (e) at different temperatures.

the internal structure of electronic component B within the temperature range of 30–200 °C. It can be seen that no remarkable changes are observed. However, it should be noted that the wires indicated by the white arrows become indistinguishable. Consequently, the (4-DMATBP)MnBr$_4$ single crystal was proven to be an excellent high-temperature scintillator with great application potential.

To further investigate the irradiation stability of the (4-DMATBP)MnBr$_4$ single crystal under X-ray excitation, we performed a long-term irradiation stability test. As displayed in Fig. S27,† after exposure to X-rays with a dose rate of 14.77 mGy s^{-1} for 300 minutes (total X-ray dosage of 133 Gy), the RL intensity of the (4-DMATBP)MnBr$_4$ single crystal remained at 91.6% of its initial value. The slight decrease in RL intensity demonstrates the robust stability of the (4-DMATBP)MnBr$_4$ single crystal in X-ray scintillation applications.

Conclusions

In summary, we successfully synthesized single crystals of (4-NH$_3$TBP)MnBr$_4$ and (4-DMATBP)MnBr$_4$ through a solvent evaporation method; the crystals show abnormal weak-TQ or ATQ behaviors originating from their rigid structure and suppressed non-radiative recombination. Notably, (4-DMATBP)MnBr$_4$ exhibits stronger ATQ ability than (4-NH$_3$TBP)MnBr$_4$. Temperature-dependent SCXRD revealed that the Mn–Mn distance of (4-DMATBP)MnBr$_4$ increases as the temperature

rises, inhibiting the Mn–Mn energy-transfer-induced emission quenching and anticipating their ATQ behavior. More importantly, TL and EPR spectra demonstrate that intrinsic defects serve as a carrier bank that can release carriers to the excited state as temperature increases and thus afford the ATQ properties of (4-DMATBP)MnBr$_4$. Further DFT calculations revealed that the defect could be ascribed to a Br-vacancy structure defect. Subsequently, we evaluated the X-ray detection performance and found that the (4-DMATBP)MnBr$_4$ single crystal exhibits a high LY of 46 722 photon per MeV at 130 °C, showing its potential for application in high-temperature detection. Benefiting from its high optical transparency and outstanding scintillation performance, the as-prepared single crystal (5 mm × 7 mm × 0.5 mm) was directly adopted as a high-temperature X-ray imaging screen. (4-DMATBP)MnBr$_4$ crystal exhibits an impressive spatial resolution of 42 lp mm^{-1} at room temperature and maintains its excellent imaging quality at high temperatures. These results suggest that the prepared OIMH single crystals are promising candidates for high-temperature X-ray detection, which could promote the development of high-temperature scintillators.

Data availability

The data supporting this article have been included as part of the ESI.† Crystallographic data for 4-NH$_3$TBPBr, 4-DMATBPBr and (4-NH$_3$TBP)MnBr$_4$ at 150 K, and (4-DMATBP)MnBr$_4$ at

different temperatures (150 K, 303 K, 403 K, 473 K, and 303 K upon cooling after thermal treatment) have been deposited at the Cambridge Crystallographic Data Centre (CCDC) under [2379301–2379308] and can be obtained from https://www.ccdc.cam.ac.uk/structures/.

Author contributions

D.-B. K. and J.-H. C. conceived and designed the experiments. J.-H. C. carried out material synthesis, measurements, and data analysis. J.-B. L., Z.-L. H., Q.-P. P., J.-H. W., Z.-Z. Z. and X.-X. G. assisted with the X-ray imaging measurements and data analysis. J.-B. L. aided in density functional theory calculations and data analysis. All authors participated in discussing the data and writing the manuscript.

Conflicts of interest

There are no conflicts to declare.

Acknowledgements

Notes and references

1 L. A. Boatner, J. S. Neal, J. A. Kolopus, J. O. Ramey and H. Akkurt, *Nucl. Instrum. Methods Phys. Res., Sect. A*, 2013, **709**, 95.

2 A. Bala, J. R. Brown, D. G. Jenkins and P. Joshi, *Nucl. Instrum. Methods Phys. Res., Sect. A*, 2021, **997**, 165161.

3 T. Wang, S. Hu, T. Ji, X. Zhu, G. Zeng, L. Huang, A. N. Yakovlev, J. Qiu, X. Xu and X. Yu, *Laser Photon. Rev.*, 2024, **18**, 2300892.

4 K. Murase, *Phys. Rev. Lett.*, 2009, **103**, 081102.

5 G. Di Sciascio, *Nucl. Part. Phys., Proc.*, 2016, **279**, 166–173.

6 L. A. Anchordoqui, *Phys. Rep.*, 2019, **801**, 1.

7 J. Asfahani, K. Samuding, R. Mostapa and O. Othman, *Appl. Radiat. Isot.*, 2021, **167**, 109296.

8 J. Qin, C. Hu, B. Lei, J. Li, Y. Liu, S. Ye and M. Pan, *J. Mater. Sci. Technol.*, 2014, **30**, 290.

9 M. Nikl and A. Yoshikawa, *Adv. Opt. Mater.*, 2015, **3**, 463.

10 E. V. D. van Loef, P. Dorenbos, C. W. E. van Eijk, K. W. Krämer and H. U. Güdel, *Nucl. Instrum. Methods Phys. Res., Sect. A*, 2002, **486**, 254.

11 Y. H. Kim, P. Arunkumar, B. Y. Kim, S. Unithrattil, E. Kim, S.-H. Moon, J. Y. Hyun, K. H. Kim, D. Lee, J.-S. Lee and W. B. Im, *Nat. Mater.*, 2017, **16**, 543.

12 F. Zhou, Z. Li, W. Lan, Q. Wang, L. Ding and Z. Jin, *Small Methods*, 2020, **4**, 2000506.

13 Z.-L. He, J.-H. Wei, J.-B. Luo, Z.-Z. Zhang, J.-H. Chen, X.-X. Guo and D.-B. Kuang, *Laser Photon. Rev.*, 2024, **18**, 2301249.

14 J.-B. Luo, J.-H. Wei, Z.-Z. Zhang, Z.-L. He and D.-B. Kuang, *Angew. Chem., Int. Ed.*, 2022, **62**, e202216504.

15 Z.-Z. Zhang, Z.-L. He, J.-B. Luo, J.-H. Wei, X.-X. Guo, J.-H. Chen and D.-B. Kuang, *Adv. Opt. Mater.*, 2024, **12**, 2302434.

16 D. Liang, H. Xiao, W. Cai, S. Lu, S. Zhao, Z. Zang and L. Xie, *Adv. Opt. Mater.*, 2023, **11**, 2202997.

17 W. Zhang, P. Sui, W. Zheng, L. Li, S. Wang, P. Huang, W. Zhang, Q. Zhang, Y. Yu and X. Chen, *Angew. Chem., Int. Ed.*, 2023, **135**, e202309230.

18 P. Dang, W. Wang, H. Lian, G. Li and J. Lin, *Adv. Opt. Mater.*, 2022, **10**, 2102287.

19 S. Wang, Y. Xu, T. Chen, W. Jiang, J. Liu, X. Zhang, W. Jiang and L. Wang, *Chem. Eng. J.*, 2021, **404**, 125912.

20 Y. Wei, H. Yang, Z. Gao, X. Yun, G. Xing, C. Zhou and G. Li, *Laser Photon. Rev.*, 2021, **15**, 2000048.

21 B.-B. Zhang, J.-K. Chen, J.-P. Ma, X.-F. Jia, Q. Zhao, S.-Q. Guo, Y.-M. Chen, Q. Liu, Y. Kuroiwa, C. Moriyoshi, J. Zhang and H.-T. Sun, *J. Phys. Chem. Lett.*, 2020, **11**, 2902–2909.

22 Y. Wei, H. Yang, Z. Gao, Y. Liu, G. Xing, P. Dang, A. A. A. Kheraif, G. Li, J. Lin and R. S. Liu, *Adv. Sci.*, 2020, **7**, 1903060.

23 Y. Wu, J. Chen, D. Zheng, X. Xia, S. Yang, Y. Yang, J. Chen, T. Pullerits, K. Han and B. Yang, *J. Phys. Chem. Lett.*, 2022, **13**, 5794–5800.

24 T.-C. Wang, S.-Y. Yao, S.-P. Yan, J. Yu, Z.-Y. Deng, A. N Yakovlev, B. Meng, J.-B. Qiu and X.-H. Xu, *ACS Appl. Mater. Interfaces*, 2023, **15**, 23421–23428.

25 Y. Wu, J. Feng, Z. Yang, Y. Liu and S. Liu, *Adv. Sci.*, 2023, **10**, 2205536.

26 Z.-Z. Zhang, J.-H. Wei, J.-B. Luo, X.-D. Wang, Z.-L. He and D.-B. Kuang, *ACS Appl. Mater. Interfaces*, 2022, **14**, 47913.

27 Z.-L. He, J.-H. Wei, Z.-Z. Zhang, J.-B. Luo and D.-B. Kuang, *Adv. Opt. Mater.*, 2023, **11**, 2300449.

28 J.-B. Luo, J.-H. Wei, Z.-L. He, J.-H. Chen, Q.-P. Peng, Z.-Z. Zhang and D.-B. Kuang, *Chem. Sci.*, 2024, **15**, 16338.

29 H. Meng, W. Zhu, Z. Zhou, R. Zhou, D. Yan, Q. Zhao and S. Liu, *J. Mater. Chem. C*, 2022, **10**, 12286.

30 Q. Qiu, G. Zhang, J. Chen, Y. Di, L. Wu, H. Chen, S. C. Chen and M. J. Lin, *Small*, 2024, **21**, 2407346.

31 H. Cui, W. Zhu, Y. Deng, T. Jiang, A. Yu, H. Chen, S. Liu and Q. Zhao, *Aggregate*, 2023, **5**, e454.

32 B. Li, J. Jin, M. Yin, K. Han, Y. Zhang, X. Zhang, A. Zhang, Z. Xia and Y. Xu, *Chem. Sci.*, 2023, **14**, 12238.

33 H. Zheng, A. Ghosh, M. J. Swamynadhan, G. Wang, Q. Zhang, X. Wu, I. Abdelwahab, W. P. D. Wong, Q.-H. Xu, S. Ghosh, J. Chen, B. J. Campbell, A. Stroppa, J. Lin, R. Mahendiran and K. P. Loh, *J. Am. Chem. Soc.*, 2023, **145**, 18549.

34 Q. Chen, J. Wu, X. Ou, B. Huang, J. Almutlaq, A. A. Zhumekenov, X. Guan, S. Han, L. Liang and Z. Yi, *Nature*, 2018, **561**, 88.

35 L. Mao, P. Guo, S. Wang, A. K. Cheetham and R. Seshadri, *J. Am. Chem. Soc.*, 2020, **142**, 13582.

36 G. Zhou, Z. Liu, J. Huang, M. S. Molokeev, Z. Xiao, C. Ma and Z. Xia, *J. Phys. Chem. Lett.*, 2020, **11**, 5956.

37 M.-S. Kwon, Y. Yu, C. Coburn, A.-W. Phillips, K. Chung, A. Shanker, J. Jung, G. Kim, K. Pipe, S.-R. Forrest,

J.-H. Youk, J. Gierschner and J. Kim, *Nat. Commun.*, 2015, **6**, 8947.

38 L.-K. Gong, Q.-Q. Hu, F.-Q. Huang, Z.-Z. Zhang, N.-N. Shen, B. Hu, Y. Song, Z.-P. Wang, K.-Z. Du and X.-Y. Huang, *Chem. Commun.*, 2019, **55**, 7303.

39 P.-R. Spackman, M.-J. Turner, J.-J. McKinnon, S.-K. Wolff, D.-J. Grimwood, D. Jayatilaka and M.-A. Spackman, *J. Appl. Crystallogr.*, 2021, **54**, 1006–1011.

40 J. Jin, K. Han, Y. Hu and Z. Xia, *Adv. Opt. Mater.*, 2023, **11**, 2300330.

41 S. He, F. Xu, T. Han, Z. Lu, W. Wang, J. Peng, F. Du, F. Yang and X. Ye, *Chem. Eng. J.*, 2020, **392**, 123657.

42 Z. Tang, R. Liu, J. Chen, D. Zheng, P. Zhou, S. Liu, T. Bai, K. Zheng, K. Han and B. Yang, *Angew. Chem., Int. Ed.*, 2022, **134**, e202210975.

43 N. Yang, J. Li, Z. Zhang, D. Wen, Q. Liang, J. Zhou, J. Yan and J. Shi, *Chem. Mater.*, 2020, **32**, 6958.

44 L. Wu, S. Sun, Y. Bai, Z. Xia, L. Wu, H. Chen, L. Zheng, H. Yi, T. Sun, Y. Kong, Y. Zhang and J. Xu, *Adv. Opt. Mater.*, 2021, **9**, 2100870.

45 W. Li, Y. Li, Y. Wang, Z. Zhou, C. Wang, Y. Sun, J. Sheng, J. Xiao, Q. Wang, S. Kurosawa, M. Buryi, D. John, K. Paurová, M. Nikl, X. Ouyang and Y. Wu, *Laser Photonics Rev.*, 2024, **18**, 2300860.

46 M.-S. Pervez, M.-F. Hossain and M.-A.-I. Nahid, *Mater. Sci. Semicond. Process.*, 2022, **137**, 106179.

47 W. Zhang, W. Zheng, L.-Y. Li, P. Huang, J. Xu, W. Zhang, Z.-Q. Shao and X.-Y. Chen, *Adv. Mater.*, 2024, **36**, 2408777.

48 W. Shao, G. Zhu, X. Wang, Z. Zhang, H. Lv, W. Deng, X. Zhang and H. Liang, *ACS Appl. Mater. Interfaces*, 2023, **15**, 932–941.